Nanoscale

Accepted Manuscript

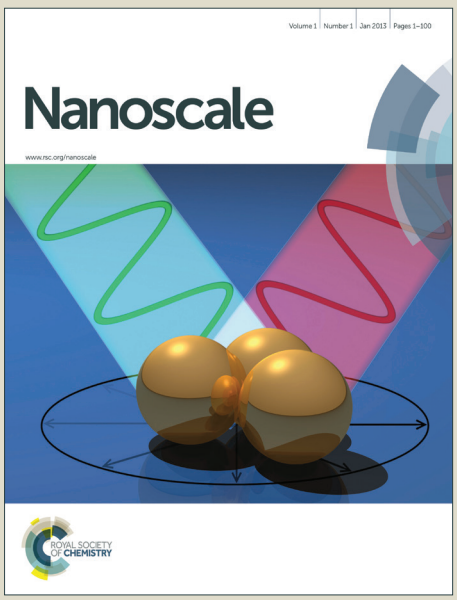

ROYAL SOCIETY OF CHEMISTRY

www.rsc.org/nanoscale

Nanoscale

RSCPublishing

ARTICLE

High Reduction of Interfacial Charge Recombination in Colloidal Quantum Dot Solar Cells by Metal Oxide Surface Passivation

Cite this: DOI: 10.1039/xoxxoooooox

Received ooth January 2014,
Accepted ooth January 2014

DOI: 10.1039/xoxxoooooox

www.rsc.org/

Jin Chang,*[a,e] Yuki Kuga,[a] Iván Mora-Seró,[b] Taro Toyoda,[a,e] Yuhei Ogomi,[c,e] Shuzi Hayase,[c,e] Juan Bisquert,[b,d] and Qing Shen*[a,e]

Bulk heterojunction (BHJ) solar cells based on colloidal QDs and metal oxide nanowires (NW) possess unique and outstanding advantages enhancing light harvesting and charge collection in comparison with planar architectures. However, the high surface area of NW structure often brings about large amount of recombination (especially interfacial recombination) and limits the open-circuit voltage in BHJ solar cells. This problem is solved here by passivating the surface of metal oxide component in PbS colloidal quantum dot solar cells (CQDSCs). By coating thin TiO_2 layers on ZnO-NW surfaces, the open-circuit voltage and power conversion efficiency have been improved over 40% in PbS CQDSCs. The transient photovoltage decay and impedance spectroscopy characterizations indicated that the interfacial recombination was significantly reduced by the surface passivation strategy. Efficiency as high as 6.13% was achieved through the passivation approach and optimization for the length of ZnO-NW arrays (device active area: 16 mm^2). All solar cells were tested under air conditions, and exhibited excellent air storage stability (without any performance decline over more than 130 days). This work highlights on the significance of metal oxide passivation in achieving high performance BHJ solar cells. The charge recombination mechanism uncovered in this work would shed light on the further improvement of PbS CQDSCs and/or other types of solar cells.

Introduction

Colloidal quantum dots (CQDs) have attracted significant attention in the last two decades due to their unique optoelectronic properties in various applications such as light emitting diodes, field effect transistors,[1] photovoltaic cells,[2, 3] photo-detectors,[4] and bio-imaging.[5] Their particular advantages in the low-temperature fabrication, solution-based processing, bandgap tunability via the quantum size effect, and the multi-exciton generation (MEG) possibility have enabled them as promising light-absorbing materials in various photovoltaic applications.[6-10]

Colloidal quantum dot solar cells (CQDSCs) – presently dominated by lead chalcogenide-based solar cells – have emerged as a new class of solar cells with efficiencies under continuous evolution and recently proved promising results on long term stability.[11, 12] Metal oxide/quantum dot heterojunction solar cells have been recently introduced and shown several advantages over previous architectures such as Schottky quantum dot solar cells.[13] This structure was initially demonstrated by Aydil and coworkers in solar cells consisting of n-type ZnO and p-type PbSe QDs.[3, 14] ZnO/PbS CQDSCs were subsequently reported by Nozik and co-workers in 2010, resulting in the first certified efficiency of 3% for this type of device.[8] The following years had seen significant increase in photovoltaic performances of CQDSCs with the development in CQD surface passivation strategies.[2, 15-18] Recently, certified efficiency of 8.6% has been reported by Bawendi and co-workers for planar ZnO/PbS CQDSCs, which further indicate the great potential of CQDSCs.[11] Although the highest efficiency was obtained using the planar structure, it does not mean that this structure is the most favourable configuration. In CQDSCs, the photocurrent density, J_{sc}, is limited by the low carrier diffusion length (< 100 nm),[19, 20] which makes that only the photogenerated charge at the depleted region plus diffusion length could be collected. This fact limits the thickness of the CQD layer (~300 nm), not sufficient to absorb all incident above-bandgap solar radiation.[20] Nanostructured TiO_2 pillars[21] and ZnO nanowire (NW) arrays[22, 23] have been explored in order to enhance the light-harvesting capacity using thicker CQD layers interpenetrated by the NW arrays. This strategy is efficient to boost the photocurrent density to values higher than 30 mA/cm^2.[23] But, on the other hand, this strategy also increases the recombination loss due to the increase of the interfacial area between NWs and CQDs, thus decreasing the device performances, especially the open circuit voltage (V_{oc}).[22, 23]

Previous investigations in CQDSCs have been mainly focused on the properties of CQDs and films. Studies on the metal oxide component have been rarely reported and mostly focused on their morphological properties and doping effect.[24-26] The surface passivation of metal oxide or interface engineering at the metal oxide/quantum dot interfaces has attracted relatively less attention, but could be similarly important. In addition, reducing the charge recombination is one of the most important ways to achieve high efficiency photovoltaic devices. Considerable emphasis has been placed on the interface recombination at the metal oxide/light absorber interfaces in various photovoltaic technologies, such as dye-sensitized solar cells (DSSCs), quantum-dot-sensitized solar cells (QDSSCs), and organic photovoltaics (OPVs).[25, 27-31] For example, TiO_2 layers were introduced by Cao and co-workers to modify the surface of mesoporous ZnO electrodes, which improved the photovoltaic performances of CdS/CdSe QDSSCs.[32] Similarly, MgO layers were also employed to modify the electrode surfaces and prevent the recombination loss in CdS QDSSCs.[33] Although the charge recombination mechanism in heterojunction CQDSCs is thought to be different from that in liquid-based QDSSCs,[25] introducing a thin passivation layer is expected to reduce the surface states of metal oxide (such as ZnO-NWs) and enhance their photovoltaic properties in CQDSCs.

Here we report the preparation of PbS CQDSC using ZnO-NWs as the selective contact for electron, improving the V_{oc} and power convention efficiency (PCE) over 40% through the metal oxide surface passivation strategy. A maximum efficiency over 6% has been achieved through the further optimization of the length of ZnO-NW arrays. The photo-generated charge recombination mechanism in CQDSCs were revealed through the open-circuit transient voltage decay measurements. Three dominated recombination paths (intrinsic recombination, interfacial recombination and direct carrier recombination) were clearly clarified for the first time. These recombination paths occur in the time scales ranging from a few μs to a few 10 ms. In addition, the prepared devices possess a remarkable long term stability over more than 130 days in air. Our results highlight the significance of metal oxide surface passivation in heterojunction CQDSCs and the elucidation of recombination mechanism in these devices, which would shed light on the further improvement of cell performances.

Experimental

Materials

Zinc acetate dehydrate ($Zn(OAc)_2 \cdot 2H_2O$, 99.9%), ethanolamine (99.0%), 2-methoxyethanol (99.0%), zinc nitrate hexahydrate ($Zn(NO_3)_2 \cdot 6H_2O$, 99.0%), hexamethylenetetramine (HMTA, 99.0%), boric acid (H_3BO_3, 99.5%), lead oxide (PbO, 99.5%), oleic acid (OA, technical grade, 60%), cadmium chloride ($CdCl_2$, 95.0%), hexadecyltrimethyl ammonium bromide (CTAB, 99.0%), and oleylamine (OLA, 99.0%) were purchased from Wako Pure Chemical Industries. Ammonium hexafluorotitanate ($(NH_4)_2TiF_6$, 99.99%), 1-octandecene (ODE, 95.0%), tetradecylphosphonic acid (TDPA, 97%), and hexamethyldisilathiane (TMS, synthesis grade) were purchased from Sigma-Aldrich. All chemicals were used as received without purification.

Preparation of ZnO-NWs

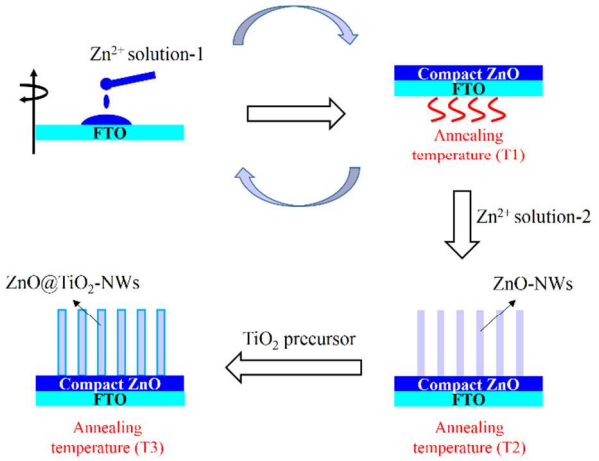

Fig. 1 Schematic illustration of the fabrication of ZnO-NWs and the surface passivation by TiO_2 coating. Zn^{2+} solution-1 contains zinc acetate and ethanolamine in 2-methoxyethanol. Zn^{2+} solution-2 is an aqueous solution containing zinc nitrate hexahydrate and hexamethylenetetramine. TiO_2 precursor is an aqueous solution containing ammonium hexafluorotitanate and boric acid.

ZnO-NW arrays were grown on FTO glasses pre-coated with compact seed layers by a modified literature method.[22] Fig. 1 illustrates the basic procedure for the synthesis of NW arrays. To prepare the sol-gel precursor for ZnO compact layer, zinc acetate dehydrate and ethanolamine were dissolved in 2-methoxyethanol to obtain 0.5 M zinc precursor (Zn^{2+} solution-1). Then, 300 μL of Zn^{2+} solution-1 was dropped on cleaned FTO glasses (25 mm × 25 mm) and spun-cast at 1000 rpm for 2 s plus 3500 rpm for 60 s, followed by baking at a temperature T1 for 10 min in air. This spin-coat and annealing processes were repeated to generate a uniform ZnO compact seed layer with thickness around 100 nm. To grow ZnO-NWs, the seed-coated FTO substrates were floated face down in Scott bottles containing the aqueous Zn^{2+} solution-2 (25 mM zinc nitrate hexahydrate and 25 mM HMTA), and heated at 90 °C for 2-4 h. After growth, the substrates were rinsed with pure water, dried with nitrogen flow, and annealed at temperature T2 for 30 min.

Preparation of ZnO@TiO_2-NWs

It is well known that ZnO nanocrystals usually possess significant amount of surface defects, as reflected by their unique defective emission in the visible light range.[34] In photovoltaic applications, the undesired defects often act as the recombination site and reduce the device performances. To reduce the surface defects of ZnO-NWs, thin TiO_2 layers were coated on ZnO surfaces because TiO_2 possesses similar band structure but less amount of defects compared with the ZnO counterpart.[35] The TiO_2 layers were grown by a chemical bath deposition (CBD) method. Typically, ZnO-NW arrays were immersed in a TiO_2 precursor containing equal molar ratio of $(NH_4)_2TiF_6$ and H_3BO_3 for 5 s at 10 °C. The concentration of TiO_2 precursor solution was adjusted in the range of 1-25 mM to optimize the thickness of TiO_2 layer. After TiO_2 coating, substrates were rinsed with pure water, dried with nitrogen flow, and annealed at temperature T3 for 30 min.

Synthesis of PbS QDs

Colloidal PbS QDs were synthesized according to a modified literature method.[2] In this work, 6 mmol PbO and 15 mmol OA

were mixed with 50 mL ODE in a 100 mL three-neck flask. The mixture was stirred and degassed at room temperature and 100 °C for 30 min and 1 h, respectively. Then, the solution was heated to 120 °C under nitrogen for another 1h, followed by the injection of TMS solution (3 mmol TMS mixed with 10 mL pre-degassed ODE) at 115 °C. After injection, the heater was removed immediately while keep stirring the solution. When the solution was cooled down to 75 °C, a $CdCl_2$-TDPA-OLA solution containing 1 mmol $CdCl_2$, 0.1 mmol TDPA, and 3 mL OLA was injected into the PbS colloidal. After cooling down to room temperature, the reaction solution was mixed with 150 mL acetone and centrifuge at 4000 rpm for 5 min to precipitate PbS QDs. The obtained precipitation was re-dispersed in 20 mL toluene, washed with 40 mL acetone followed by centrifugation. This purification process was repeated twice to remove the unbound OA ligands in PbS colloidal. After purification, the obtained PbS QD precipitation was dried by nitrogen flow and dispersed in 15 mL octane. The concentration of PbS colloidal was approximately 50 $mg \cdot mL^{-1}$ assuming that the reactant TMS was completely transformed into the PbS product.

Fabrication of PbS CQDSCs

To fabricate PbS heterojunction solar cells, PbS colloidal QDs were deposited on ZnO-NW and ZnO@TiO_2-NW arrays by a typical layer-by-layer method using a fully automatic spin-coater. Each spin-coating cycle consists of three steps: PbS deposition, ligand exchange, and solvent rinse. Generally, PbS colloidal (100 μL) was dropped on NW array-coated FTO substrates and spun-cast at 2500 rpm for 15 s. Then, CTAB solution (30 mM in methanol) was dropped onto the substrate and spun dry after a 60 s wait. The ligand exchange step was conducted twice to ensure complete ligand exchange with the oleic acid capped on PbS surfaces. The substrate was then rinsed three times with methanol to remove excess unbound ligands. For typical ZnO/PbS solar cells, this spin-cast process was repeated 20-25 cycles depending on the length of NW arrays. Finally, a 100 nm Au contact was thermally evaporated on the PbS layer through a mask to create four identical cells on each substrate. Control solar cells with the planar architecture were fabricated by spin-coating PbS layers on compact ZnO layers with identical methods as described above. The thickness of ZnO and PbS layers were 100 nm and 300 nm, respectively.

Device Characterization

The current density-voltage (*J-V*) measurements were performed using a Keithley 2400 source meter under dark and AM 1.5G irradiation (100 mW/cm^2), respectively, with a Peccell solar simulator PEC-L10. The IPCE spectra were measured under illumination using a Nikon G250 monochromator equipped with a 300 W Xe arc lamp. The transient open-circuit voltage decay measurements were carried out using a 532 nm diode laser with the pulse duration of 5 ns and repetition rate of 4 Hz. The voltage responses were recorded using an Iwatsu digital oscilloscopes DS-5554. The transient voltage decay measurements were taken without a background light bias. The electrochemical impedance spectroscopy (EIS) measurements were performed under dark conditions using an impedance analyser (BioLogic, SP-300) by applying a small voltage perturbation (10 mV rms) at frequencies from 1 MHz to 0.1 Hz for different forward bias voltages.

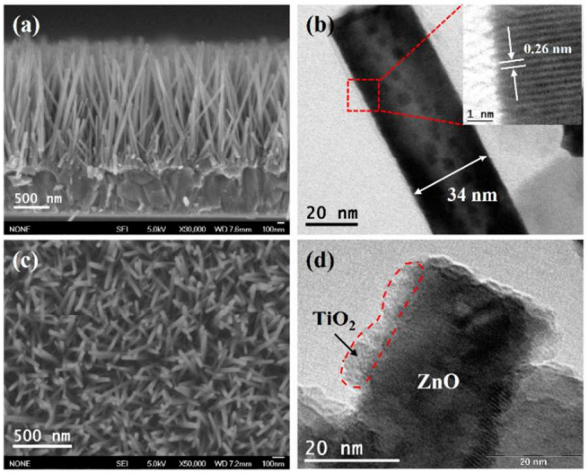

Fig. 2 (a) Side view SEM image of ZnO-NW arrays with a length of approximately 1.6 μm; (b) TEM image of bare ZnO-NW with a diameter of 34 nm; the inset HR-TEM image shows the interplanar distance of 0.26 nm along *c*-axis; (c) Top view SEM image of ZnO@TiO_2-NW arrays; (d) TEM image of ZnO@TiO_2-NW, showing ZnO surfaces coated with TiO_2 layer with the thickness of 3-5 nm.

Other characterization

The morphology of ZnO-NWs and ZnO@TiO_2-NWs were examined by a scanning electron microscopy (SEM, JEOL, JSM-6340) and a transmission electron microscopy (TEM, JEOL, JEM-2010). The elemental composition of ZnO@TiO_2-NWs was determined by the scanning electron microscopy equipped with an energy dispersive x-ray (EDX) spectroscope. The UV-vis-NIR absorption spectra of NW arrays and PbS QDs were investigated with a spectrophotometer (JASCO, V-670). The florescence spectra of NW arrays were measured by a spectrofluorometer (JASCO, FP-6500). The average size of PbS QDs was determined by a transmission electron microscopy (TEM, JEOL, JEM-2010). The photoelectron yield spectra of ZnO and PbS films were measured by an ionization energy measurement system (Model BIP-KV205, Bunkoukeiki Co, Ltd.).

Results and Discussion

Growth and surface passivation of ZnO-NWs

To obtain homogeneous metal oxide/PbS bulk heterojunction with high electron collection efficiency, uniform metal oxide nanostructure with minimum surface defects are required. In this work, ZnO-NW and ZnO@TiO_2-NW (TiO_2 passivated ZnO-NW) arrays were prepared by wet-chemical methods as illustrated in Fig. 1. The annealing temperatures (T1, T2 and T3 as shown in Fig. 1) for each preparation step and the TiO_2 precursor concentration were optimized to achieve uniform NW arrays with minimum surface defects. After coating zinc solution-1 on FTO substrates, the obtained ZnO compact layers were annealed at 150 °C in air (see optimization details in support information), followed by the growth of ZnO-NWs in zinc solution-2. The side view SEM image of optimized ZnO-NWs is shown in Fig. 2a, with a length approximately 1.6 μm. Fig. 2b displays the corresponding TEM and high resolution transmission electron microscopy (HR-TEM) images, showing

the NWs are 34 nm in diameter and 0.26 nm interplanar distances along c-axis of ZnO-NWs.

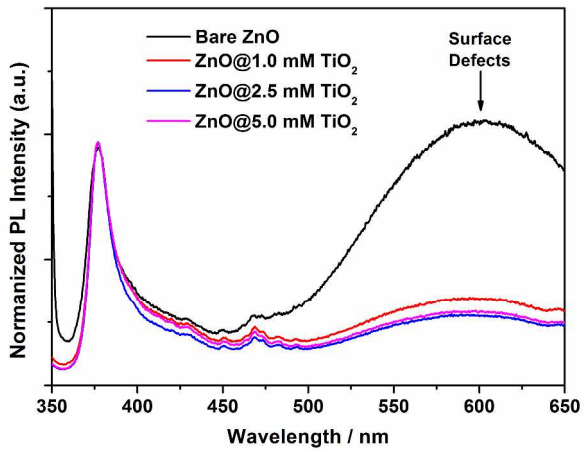

Fig. 3 Room temperature PL spectra of bare ZnO-NW arrays and the arrays treated with TiO_2 precursors with different concentrations (1.0, 2.5 and 5.0 mM) at 10 °C for 5 s.

For the surface passivation of ZnO-NWs, thin TiO_2 layers were grown onto ZnO surfaces by immersing the arrays into an aqueous TiO_2 precursor containing $(NH_4)_2TiF_6$ and H_3BO_3. TiO_2 layers were obtained through the etching of ZnO and the chemical reaction between ZnO and TiO_2 precursor according to the following equation:[36]

$$ZnO + 2TiF_6^{2-} + 2H_3BO_3 \rightarrow Zn^{2+} + 2TiO_2 + 4F^- + 2BF_4^- + 3H_2O$$

As shown in above equation, one portion of ZnO can be dissolved in TiF_6^{2-}/H_3BO_3 solutions to form two portions of TiO_2 in situ. Therefore, the average diameter of ZnO-NWs would be slightly increased after TiO_2 treatment, depending on the dissolution degree of ZnO-NWs. Meanwhile, the roughness of ZnO surfaces would also be increased due to the etching of TiO_2 precursor on ZnO. To minimize the effect of TiO_2 treatment on ZnO morphologies, TiO_2 precursor with low concentrations (1.0, 2.5 and 5 mM) were employed to treat ZnO-NWs. High concentration precursors were employed as control experiments, which exhibited poor device performances. Fig. 2c presents the top view SEM image of ZnO-NWs arrays treated with 5 mM TiO_2 precursor, which shows similar diameter with bare ZnO-NWs. The Energy Dispersive X-ray Spectroscopy (EDX) image shown in Fig. S2 confirmed the formation of TiO_2 after annealing. The TEM image of ZnO@TiO_2-NWs is shown in Fig. 2d. It was obviously shown that the ZnO surfaces were coated with a rough TiO_2 layer with thickness in the range of 3-5 nm.

To evaluate the effects of annealing temperatures and surface passivation on ZnO surface defects, room-temperature photoluminescence (PL) studies were carried out for obtained samples. Firstly, as prepared bare ZnO-NWs were annealed at temperature T2 (300 - 450 °C, see Fig. 1) to investigate the effect of annealing temperature on the PL spectra of ZnO-NWs. As displayed in Fig. S3, all ZnO-NWs samples exhibited a narrow UV emission at approximately 378 nm, which can be attributed to the near band edge transitions in ZnO. A broad visible emission centered at around 600 nm could be attributed to the oxygen vacancies on ZnO surfaces.[37] The PL spectrum of the as-prepared ZnO-NWs was similar with that of the samples annealed at 300 °C and 350 °C, except a slight red-shift of the visible emission for annealed samples. As the annealing temperature was increased to 400 - 450 °C, the surface defect-originated emission was highly increased with a consequent decrease for the UV emission. Therefore, the optimal annealing temperature was determined as 350 °C for the sake of lowest defect emission and sufficient ZnO crystallinity. The annealed ZnO-NWs were then treated with TiO_2 precursors, followed by annealing at temperature T3 (see Fig. 1) for 30 min. Similarly, the annealing temperature T3 was also optimized as 350 °C, as shown in Fig. S4. The effect of TiO_2 treatment on the PL spectra of ZnO-NWs is shown in Fig. 3. After TiO_2 passivation, the intensity of the visible emission was dramatically decreased, suggesting that the defects on ZnO surfaces were largely eliminated by the TiO_2 layer. Note that slight variation in passivation is observed by changing the precursor concentration. The reduction in the surface defects of ZnO-NWs could be mainly due to the fact that TiO_2 usually possesses less amount of surface states compared with ZnO.[35]

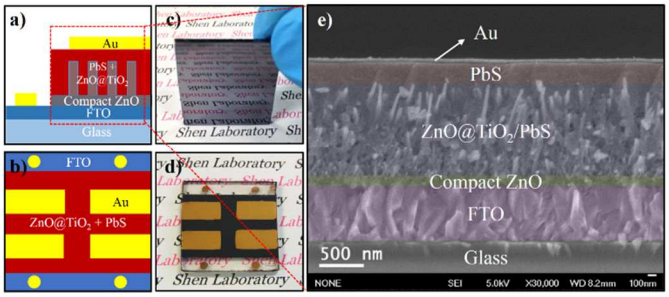

Fig. 4 (a, b) The schematic illustration of ZnO@TiO2/PbS solar cells; (c, d) photographs of the PbS CQDSCs before and after the deposition of Au contacts; (e) a typical cross-section SEM image of ZnO@TiO2/PbS solar cells.

Characterization and photovoltaic performance of PbS CQDSCs

PbS CQDSCs based on ZnO-NWs and ZnO@TiO_2-NWs were fabricated by the layer-by-layer spin coating method with ligand exchange.[2] Oleic acid (OA)-capped colloidal PbS QDs were spun cast on FTO substrates with NW arrays. Cetyltrimethylammonium bromide (CTAB) solution was applied for the solid state ligand exchange of PbS films, followed by the rinse step to remove unbound excess ligands. TEM image shows that the average size of PbS QDs employed in this work is approximately 3.5 nm (Fig. S5a). The first exciton absorption peak of OA-capped PbS was 1040 nm for both colloidal and thin films. A red shift was observed after ligand exchange with CTAB (Fig. S5b), indicating the enhanced interaction between closely packed PbS QDs.[38] The spin coat cycles were repeated until NW arrays were filled by PbS QDs, obtaining an overlayer of approximately 200 nm on top of arrays. Au electrodes with thickness of approximately 100 nm was deposited on PbS layer by a thermal evaporation method. Fig. 4a, b illustrate the structure of ZnO@TiO_2/PbS solar cells employed in this work, with four parallel cells on each FTO substrate. Fig. 4c, d display the photographs of PbS CQDSCs before and after the deposition of Au contacts, showing the mirror-like PbS film fabricated in our laboratory. The cross-section SEM image of fabricated cells is presented in Fig. 4e, which confirmed the bulk heterojunction structure of fabricated cells. It also shows that PbS QDs have successfully infiltrated and evenly distributed between the NW arrays. We

observed that the fabrication of void-free PbS films was necessary to achieve high efficiency solar cells. High spin-coat speed (at least 2500 rpm) for PbS colloidal and enough spun-dry time (15 s) were critical to obtain void-free PbS films. The

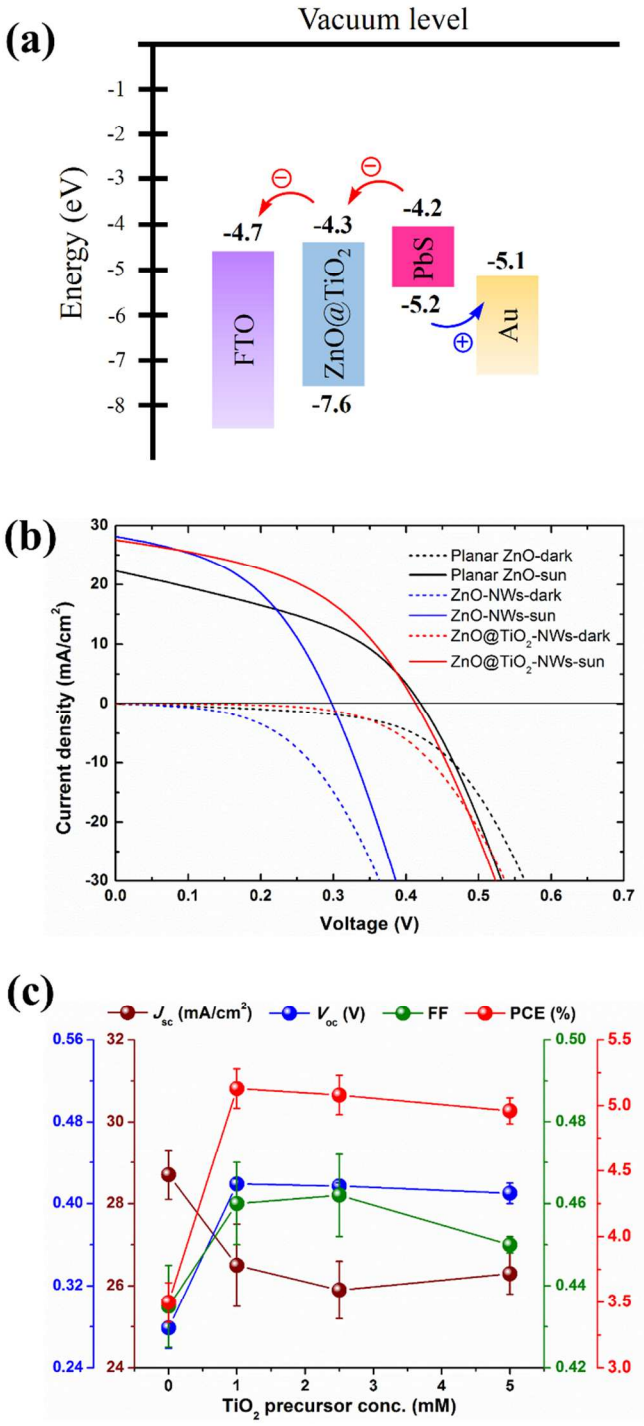

Fig. 5 (a) Schematic energy level diagram of FTO/ZnO@TiO_2/PbS/Au solar cells. (b) Comparison of the photocurrent density-voltage (*J-V*) curves of PbS CQDSCs based on planar ZnO and ZnO-NWs with or without TiO_2 treatment. (c) Effects of TiO_2 precursor concentration on the J_{sc}, V_{oc}, FF, and PCE values of ZnO-NWs/PbS CQDSCs.

active area under illumination was defined as 16 mm^2 (4 mm × 4 mm) by a photomask. Note that the active area is significantly larger than typical values (~1-5 mm^2) reported in previous literatures.[11, 15, 22, 23]

Fig. 5a shows the diagram of energy level alignment in FTO/ZnO@TiO_2/PbS/Au solar cells. The energy levels of ZnO and PbS were estimated from the photoelectron yield spectroscopy (PYS) and UV-vis-NIR measurements (Fig. S5, S6 and S7), while the work function values of FTO and Au were taken from published literature.[23] Control planar samples (PCE = 3.8%, J_{sc} = 22.3 mA/cm^2, V_{oc} = 0.42 V, and fill factor (FF) = 0.41) were prepared. Compared with planar PbS CQDSC, bare ZnO-NW device exhibited higher J_{sc} values, but relatively lower V_{oc}, in accordance with our expectation, while both present similar FF (Fig. 5b). Notably, through the surface passivation approach, the V_{oc} of ZnO-NW based solar cell was significantly improved from approximately 0.3 V up to 0.42 V without obvious decline in J_{sc} (Fig. 5b). This means that declined V_{oc} value caused by the increased interface area of NWs were well-recovered by the surface passivation approach. Consequently devices prepared with properly passivated ZnO-NWs present significantly higher photocurrent and similar V_{oc} for a higher final performance in comparison with planar architecture. Plots in Fig. 5c shows the detailed effects of TiO_2 treatment on the J_{sc}, V_{oc}, fill factor (FF), and PCE of ZnO-NWs-based PbS CQDSCs. It was shown that V_{oc} was highly improved from approximately 0.3 V for bare ZnO cell up to 0.42 V for ZnO@TiO_2 cells, around 40% enhancement. The PCE was enhanced basically in the same scale from 3.5% to 5%, as the decrease observed in photocurrent is compensated by an increase of FF.

Note that both planar and NW architectures present low FF, this fact cannot be attributed to the cell configuration but to the QD preparation. Further organic, inorganic or hybrid passivation of colloidal QDs will help to enhance this parameter.[15] Passivation of QDs will also enhance the V_{oc}. However the use of nanowires points to the photocurrent enhancement and subsequent use of passivation removes the deleterious effect introduced by the enhanced recombination.

The slight decrease in J_{sc} after TiO_2 treatment could be attributed to the fact that TiO_2 layers probably affected the electron injection from PbS QDs to ZnO-NWs because TiO_2 possesses relatively lower electron mobility than ZnO-NWs.[34, 39] This was supported by our observation that J_{sc} decreased dramatically when higher concentration TiO_2 precursors and/or longer treatment time were employed (see Fig. S8 and Table S1). It is noted that the J_{sc} value was nearly same as the TiO_2 precursor concentration was in the range of 1.0 - 5.0 mM, except the lower value in the case of 2.5 mM. This could be due to the structural complexity of bulk heterojunction CQDSCs. Slight deviation in photovoltaic performances might occur if any voids exist within PbS films, although identical fabrication procedures were strictly controlled in our work. Nevertheless, it can be seen that the J_{sc} value was reduced after TiO_2 treatment for ZnO-NW arrays, and the effect was more obvious in the case of higher TiO_2 precursor concentrations. The incident photon-to-current efficiency (IPCE) spectra of fabricated cells are exhibited in Fig. S9, with the calculated photocurrent consistent with the measured J_{sc} values. ZnO@TiO_2/PbS devices exhibited relatively lower IPCE values than that in the bare ZnO/PbS device at longer wavelengths, which was consistent with the *J-V* results. Since the light is incident from FTO, long-wavelength photons are able to penetrate deeper in solar cells due to the smaller absorption coefficient of PbS QDs

at longer wavelengths (Fig. S5b). Electrons generated by long-wavelength photons have to transport a long distance to arrive at FTO substrate along the NW arrays. The decrease of IPCE in ZnO@TiO_2/PbS devices at longer wavelengths indicated a lower photocurrent collection efficiency in comparison with that of bare ZnO/PbS device.

The difference of photovoltaic properties between bare ZnO/PbS and surface-passivated ZnO@TiO_2/PbS cells could

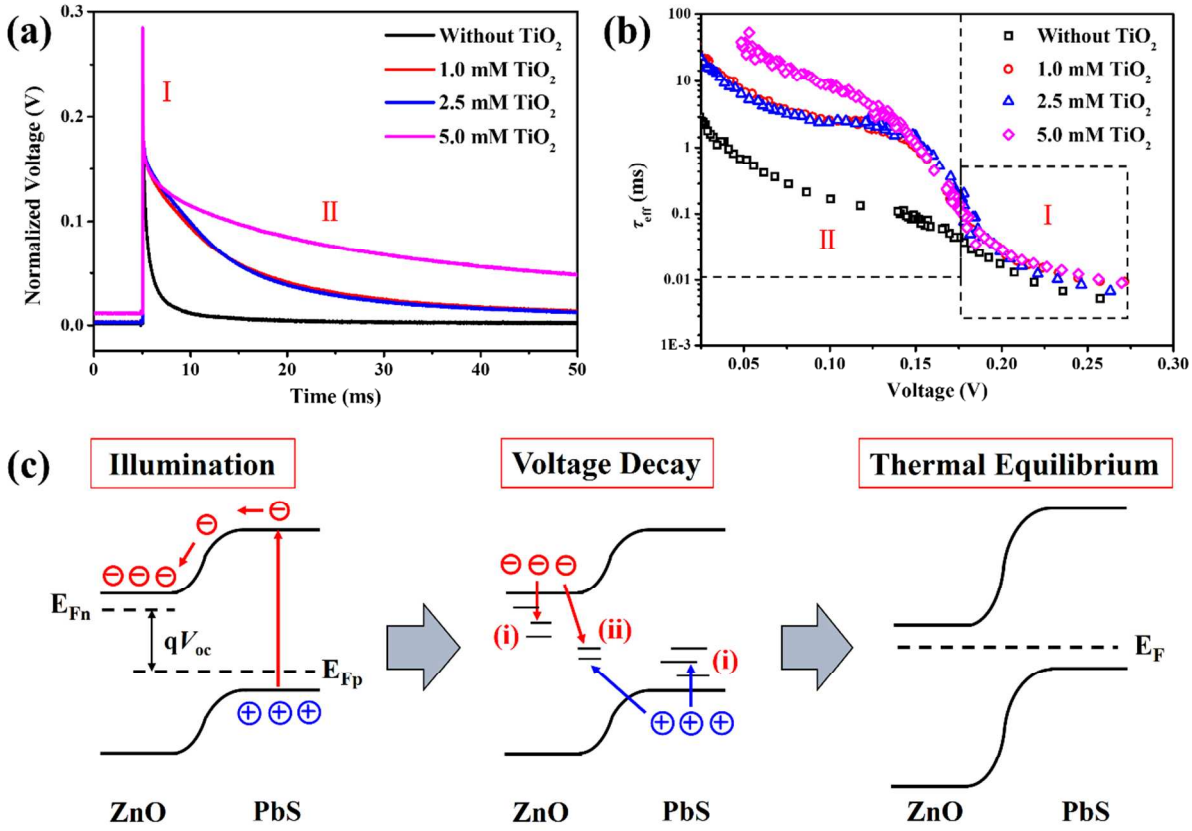

Fig. 6 (a) Normalized open-circuit photovoltage decay curves of ZnO/PbS CQDSCs with and without the TiO_2 coating for ZnO-NWs, showing two dominant decay processes. (b) The effective carrier lifetime calculated from the voltage decay curves. (c) Schematic illustration of the energy level alignment in PbS CQDSCs during the voltage decay measurement. The voltage decay process is mainly attributed to two recombination paths: i) intrinsic trapping-assisted recombination in ZnO and PbS films; ii) interfacial recombination at ZnO/PbS interfaces.

also be observed from the dark current curves as shown in Fig. 5b. The obtained PbS quantum dot solar cells show a clearly decrease in overall dark current upon the surface passivation of ZnO. This decrease could be attributed to the reduction of recombination at the ZnO@TiO_2/PbS interface, because dark current in p-n junction solar cells is mainly dominated by the recombination close to the junction.[25] High density defect at the ZnO/PbS interface would allow carriers to move to these recombination sites very quickly and recombine, thus increase the dark current.

To explore the mechanism of the photovoltaic enhancement in surface passivated ZnO/PbS solar cells, transient open-circuit photovoltage decay measurements were carried out. Through investigating the open-circuit photovoltage decay behaviour, the charge recombination mechanism in solar cells could be extracted. Upon illumination, photo-generated electrons were injected from PbS QDs to ZnO-NWs while holes remained in PbS QD films, forming the photovoltage V_{oc} within ZnO/PbS junctions under open-circuit conditions. When incident light is switched off, photo-generated charges would recombine in various paths, leading to the decay of V_{oc} until recovering to the thermal equilibrium state (see the illustration in Fig. 6c). Fig. 6a shows the transient photovoltage decay curves of our PbS CQDSCs. It was obviously shown that ZnO@TiO_2/PbS cells exhibited much slower decay processes than that of bare ZnO/PbS cell, which provided a direct proof of the reduced recombination in the surface-passivated cells. In addition, the decay curves could be roughly divided into two sections: (i) a very fast decay process occurred in the initial stage; (ii) a slow decay process with the sample-dependent timescale. To quantitatively analyse the voltage decay processes, the voltage decay curves were fitted with a two exponential decay plus an offset according to the following equation:

$$y(t) = A_1 e^{-t/\tau_1} + A_2 e^{-t/\tau_2} + A_3 \quad (1)$$

where A_1, A_2 and A_3 are proportionality constants, τ_1 and τ_2 are time constants. The fitted curves and the corresponding parameters are shown in Fig. S10 and Table 1, respectively. For equation (1), we assigned the first exponential decay to the fast voltage decay process (section 1), while the second exponential decay and offset correspond to the slow voltage decay process (section 2). According to fitted data, the time constant τ_1 was similar for passivated and non-passivated cells considering the ultrafast timescale and fitting uncertainty. Notably, the weight of A_1 was decreased from 76% to 39% after the surface passivation of ZnO. This could be due to the reduction of surface defects in passivated ZnO (as supported by the PL results in Fig. 3), i.e., the reduction of electron trapping on ZnO surfaces. The remaining A_1 weight (approximate 40%) probably corresponds to the hole trapping in PbS QDs and remaining electron trapping in ZnO. For the slow voltage decay process, time constant τ_2 was obviously increased from 3.23 ms to 17.6 ms after ZnO passivation. The prolonged charge recombination process in passivated cells was mainly attributed to the reduced interfacial recombination at ZnO/PbS interfaces.

Table 1 Fitted proportionality constants (including the relative weight) and time constants obtained from open-circuit photovoltage decay curves of PbS CQDSCs.

Cells	A_1 (A_1/(A_1+A_2+A_3))	τ_1 (ms)	A_2 (A_2/(A_1+A_2+A_3))	τ_2 (ms)	A_3 (A_3/(A_1+A_2+A_3))
w/o TiO_2	0.15 (76%)	0.044 ±0.002	0.044 (22%)	3.23 ± 0.03	0.0032 (1%)
1.0 mM TiO_2	0.11 (41%)	0.062 ± 0.0005	0.14 (52%)	8.81 ± 0.01	0.015 (7%)
2.5 mM TiO_2	0.11 (40%)	0.037 ± 0.0005	0.15 (55%)	8.37 ± 0.006	0.014 (5%)
5.0 mM TiO_2	0.09 (39%)	0.18 ± 0.02	0.098 (42%)	17.6 ± 0.05	0.043 (19%)

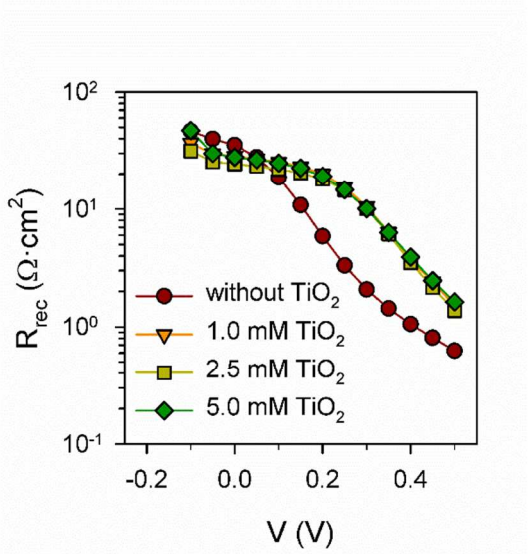

Fig. 7 Recombination resistance obtained from impedance spectroscopy analysis.

In addition to the voltage decay analysis, we also evaluated the recombination processes based on the effective carrier lifetime (τ_{eff}), which can be defined as the follow equations (see details in the supporting information):[40, 41]

$$\tau_{eff} = -\left(\frac{kT}{q}\right) / \left(\frac{dV_{oc}}{dt}\right) = 1/(\tau_n^{-1} + \tau_p^{-1}) \quad (2)$$

$$\tau_n^{-1} = \frac{(dn/dt)}{n} \quad (3)$$

$$\tau_p^{-1} = \frac{(dp/dt)}{p} \quad (4)$$

where k is the Boltzmann constant, T is the temperature, q is the elementary charge, n is free electron density in ZnO-NWs, p is free hole density in PbS QDs. τ_n and τ_p are free electron lifetime in ZnO-NWs and free hole lifetime in PbS QDs, respectively. According to above equations, the open-circuit photovoltage decay is dependent on both the electron and hole lifetimes in p-n junction CQDSCs.

As shown in Fig. 6b, the photovoltage-dependent effective carrier lifetime could also be divided into two sections, corresponding to the two photovoltage decay processes, respectively. In the high V_{oc} regime (section I in Fig. 6b), the value of τ_{eff} was below 0.1 ms and nearly same for both passivated and non-passivated devices. We propose that this regime could be assigned to a bulk recombination mechanism. In the low V_{oc} regime (section II in Fig. 6b), the values of τ_{eff} in

passivated cells were 1-2 orders higher than that of non-passivated cell. This confirmed again that the second voltage decay process was dominated by the interfacial recombination at ZnO/PbS interfaces. Based on above experimental results, it was concluded that the surface passivation of metal oxide films significantly reduced the interfacial recombination, thus enhancing the V_{oc} and PCE in ZnO/PbS CQDSCs. According to our voltage decay analysis, bulk recombination has to be reduced using other strategies as QD passivation.[15]

In addition to the transient photovoltage decay measurements, impedance spectroscopy measurements were also conducted to verify the reduction of interfacial recombination in passivated ZnO/PbS CQDSCs. The impedance technique has been extensively employed for the characterization of a variety of photovoltaic devices,[42-44] but it has not been employed significantly in the characterization of CQDSCs. This technique allows to easily obtain the recombination resistance, R_{rec}, which is inversely proportional to the recombination rate. Fig. 7 shows a clear enhancement of R_{rec} after coating TiO_2 on ZnO-NW surfaces, indicating a reduction of the recombination rate and causing the increase in V_{oc} observed for these devices. This result was consistent with the voltage decay analysis as discussed above.

Effect of the NW Length and Device Stability.

In addition to the surface passivation, the effect of NW length on the photovoltaic performance of ZnO@TiO_2/PbS cells was also investigated. It is known that bulk heterojunction PbS cells possess the advantage of high light absorption and effective carrier extraction owing to their nanostructures with short carrier diffusion length. As the device thickness increases, the light harvest can be enhanced; however, the photo-generated current density often decreases when the thickness is beyond the limitation of effective carrier collection. Considering these effects, it is significant to optimize the length of NW arrays in our ZnO@TiO_2/PbS devices.

Fig. S12 shows the cross-section SEM images of ZnO-NW arrays grown on FTO substrates, with growth times varying from 2 to 4 hours. Short ZnO-NWs with length about 400 nm was obtained when the growth time was 2 h. When the growth time was prolonged to 3, 3.5, and 4 h, the corresponding ZnO-NWs with the length of 1000 nm, 1400 nm, and 1600 nm were obtained, respectively. ZnO-NWs with different length were then immersed in a 1.0 mM TiF_6^{2-}/H_3BO_3 solutions for 5 s to form ZnO@TiO_2-NWs. After TiO_2 treatments, PbS CQDSCs were fabricated with the same procedure as described before (see details in the experimental section). Fig. 8a illustrates the photogenerated carrier collection in ZnO@TiO_2/PbS solar cells. Fig. 8b shows the *J-V* curves of PbS CQDSCs with different length of ZnO@TiO_2-NW arrays. The detailed effects of NW length on the J_{sc}, V_{oc}, FF, and PCE are displayed in Fig. 8c. When the NW length was increased from 0.4 μm to 1 μm, J_{sc} was increased from approximately 15 to over 30 mA/cm^2. This could be due to the increase of PbS QDs loading in longer NW arrays, leading to the enhancement in light harvesting. Then, Jsc slightly decreased as the NW length was increased further to 1.6 μm. This could be attributed to a decrease in charge collection efficiency as the length of NW array increasing. Similarly, FF values decreased as increasing the NW length, which could be mainly attributed to the increase of resistances and surface defects in NWs. By contrast, the V_{oc} values were independent with the NW length. The highest PCE of 6.13% was obtained for the cell with NW length of 1 μm, which was the best result for PbS CQDSCs based on ZnO-NWs. The corresponding IPCE spectra are shown in Fig. 8d, with the calculated photocurrent consistent with the measured J_{sc} values.

In addition to cell efficiencies, the stability and reproducibility are also important factors for the overall evaluation of solar cells. Hysteresis has been identified as a big problem for the correct determination of cell efficiency in various types of photovoltaic devices. Therefore, we have carefully evaluated the hysteresis in our PbS CQDSCs, as

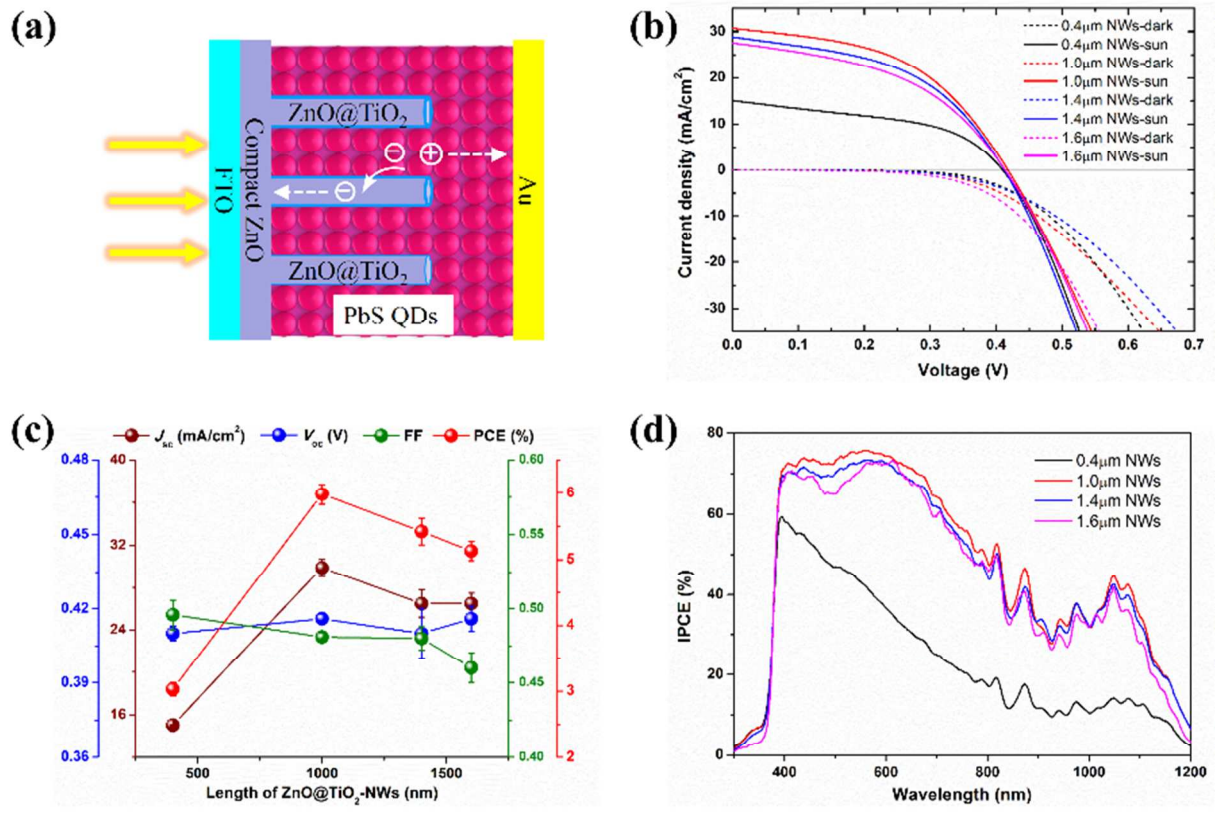

Fig. 8 (a, [illegible]) with different NW length. (c) Effects of the NW length on the J_{sc}, V_{oc}, FF and PCE of PbS CQDSCs. (d) IPCE spectra of ZnO@TiO_2/PbS cells with different length of NW arrays, with the calculated photocurrent consistent with the measured J_{sc} values.

shown in Fig. 9b and Fig. S13. No significant hysteric effect (lower than 1%) has been identified in our CQDSC devices. Furthermore, we have evaluated the long term stability of the prepared devices. As can be seen in Fig. 9a, both ZnO/PbS and ZnO@TiO_2/PbS devices exhibited excellent long-term storage stability for over 130 days (> 3000 h). All solar cells were stored and tested in the ambient atmosphere. During the course of stability assessment, cells were stored in air under dark conditions without the control of humility. All photovoltaic parameters exhibited overall increase as the storage time continued. The most interesting part is that J_{sc} and FF in ZnO/PbS and ZnO@TiO_2/PbS devices approached to the same values after storing for over 60 days. By contrast, the difference in V_{oc} was narrowed during the initial 40 days, then constantly kept around 0.09 V. The improvement in V_{oc}, therefore, enhanced the PCE value in ZnO@TiO_2/PbS cells and maintained, even enhanced for a long term.

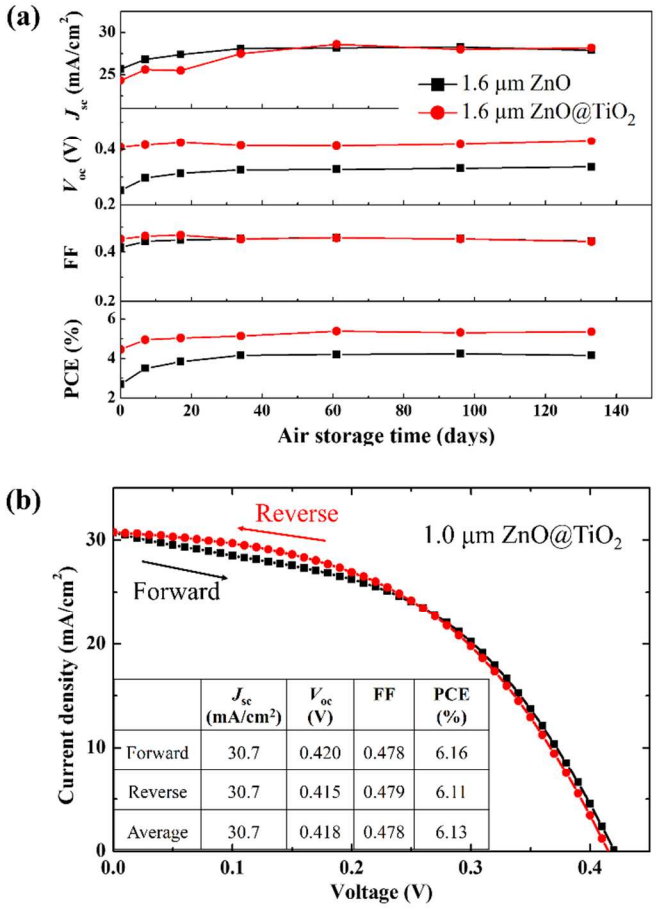

	J_{sc} (mA/cm^2)	V_{oc} (V)	FF	PCE (%)
Forward	30.7	0.420	0.478	6.16
Reverse	30.7	0.415	0.479	6.11
Average	30.7	0.418	0.478	6.13

Fig. 9 (a) Stability evaluation of bare and surface-passivated PbS CQDSCs with 1.6 μm length NW arrays. All devices were stored and tested in ambient atmosphere. (b) *J-V* curves of a NW length-optimized ZnO@TiO_2/PbS cell measured by forward (short circuit → open circuit) and reverse (open circuit → short circuit) scans with 10 mV voltage steps and 200 ms delay times under AM 1.5 G illumination.

Conclusion

In summary, we have confirmed the beneficial role of ZnO NWS in order to enhance solar CQDSC photocurrent. In addition, We have significantly improved the photovoltaic performances of PbS BHJ CQDSCs by introducing passivation layers on electron-selective substrates (ZnO-NWs), which was proved to reduce the interfacial recombination at ZnO/PbS interfaces. The surface defects of ZnO-NWs were significantly reduced by coating 3-5 nm thick TiO_2 layers on ZnO surfaces and annealing NW arrays at an optimized temperature (350 °C). Our results show that low TiO_2 precursor concentration (1-5 mM) was powerful to passivate ZnO-NWs and improve photovoltaic properties, while high precursor concentration (> 12.5 mM) was detrimental to our devices. A dramatic improvement (over 40%) in V_{oc} and PCE was finally achieved through the optimized surface passivation strategy for ZnO-NWs arrays.

The mechanism behind this achievement was explored through the open-circuit voltage decay and impedance spectroscopy techniques. It was revealed that the metal oxide passivation strategy significantly reduced the interfacial recombination in PbS CQDSCs. This conclusion was supported by impedance spectroscopy characterization, which shows increased recombination resistance in passivated solar cells. By analysing the voltage decay curves, we observed that bulk recombination in QD layer is another bottleneck in CQDSCs performance, which accounts for approximately 40% of total charge recombination. Colloidal QD passivation should reduce this recombination as it has been previously reported. Consequently even higher efficiencies could be expected in the next future for CQDSCs NW architectures. Through the metal oxide passivation strategy and the optimization of ZnO-NWs length, maximum efficiency of 6.13% has been achieved, which is currently the highest efficiency for PbS CQDSCs based on ZnO-NWs. This result is quite outstanding in consideration of the active area (16 mm^2), which is much larger than those used in previous literatures. The device stability and measurement method were also evaluated, which show negligible hysteric effect in our devices and excellent storage stability in air (without any performance decline over 130 days). In short, this study highlights the significance of metal oxide passivation in achieving high efficiency bulk heterojunction solar cells. The charge recombination mechanism characterized in this work would shed light on the further improvement of PbS CQDSCs and/or other types of solar cells.

Acknowledgements

This research was supported by the Japan Science and Technology Agency (JST) CREST program and MEXT KAKENHI Grant Number 26286013.

Notes and references

[a] Faculty of Informatics and Engineering, The University of Electro-Communications, 1-5-1 Chofugaoka, Chofu, Tokyo 182-8585, Japan. Email: jin@jupiter.pc.uec.ac.jp; shen@pc.uec.ac.jp. Tel: +81 42 443 5471. Fax: +81 42 443 5501.

[b] Photovoltaic and Optoelectronic Devices Group, Department de Física, Universitat Jaume I, 12071 Castelló, Spain.

[c] Faculty of Life Science and Systems Engineering, Kyushu Institute of Technology, 2-4 Hibikino, Wakamatsu-ku, Kitakyushu, Fukuoka 808-0196, Japan.

[d] Department of Chemistry, Faculty of Science, King Abdulaziz University, Jeddah, Saudi Arabia

[e] CREST, Japan Science and Technology Agency (JST), 4-1-8 Honcho, Kawaguchi, Saitama 332-0012, Japan

Electronic Supplementary Information (ESI) available: [details of any supplementary information available should be included here]. See DOI: 10.1039/b000000x/

1 J.-S. Lee, M. V. Kovalenko, J. Huang, D. S. Chung and D. V. Talapin, *Nat. Nanotech.*, 2011, **6**, 348-352.
2 J. Tang, K. W. Kemp, S. Hoogland, K. S. Jeong, H. Liu, L. Levina, M. Furukawa, X. Wang, R. Debnath, D. Cha, K. W. Chou, A. Fischer, A. Amassian, J. B. Asbury and E. H. Sargent, *Nat. Mater.*, 2011, **10**, 765-771.
3 K. S. Leschkies, T. J. Beatty, M. S. Kang, D. J. Norris and E. S. Aydil, *ACS Nano*, 2009, **3**, 3638-3648.
4 G. Konstantatos, I. Howard, A. Fischer, S. Hoogland, J. Clifford, E. Klem, L. Levina and E. H. Sargent, *Nature*, 2006, **442**, 180-183.
5 K. Zagorovsky and W. C. W. Chan, *Nat. Mater.*, 2013, **12**, 285-287.
6 H. Lee, H. C. Leventis, S.-J. Moon, P. Chen, S. Ito, S. A. Haque, T. Torres, F. Nüesch, T. Geiger, S. M. Zakeeruddin, M. Grätzel and M. K. Nazeeruddin, *Adv. Funct. Mater.*, 2009, **19**, 2735-2742.
7 G. I. Koleilat, L. Levina, H. Shukla, S. H. Myrskog, S. Hinds, A. G. Pattantyus-Abraham and E. H. Sargent, *ACS Nano*, 2008, **2**, 833-840.
8 J. M. Luther, J. Gao, M. T. Lloyd, O. E. Semonin, M. C. Beard and A. J. Nozik, *Adv. Mater.*, 2010, **22**, 3704-3707.
9 A. Luque, A. Martí and A. J. Nozik, *MRS Bull.*, 2007, **32**, 236-241.
10 O. E. Semonin, J. M. Luther, S. Choi, H.-Y. Chen, J. Gao, A. J. Nozik and M. C. Beard, *Science*, 2011, **334**, 1530-1533.
11 C.-H. M. Chuang, P. R. Brown, V. Bulović and M. G. Bawendi, *Nat. Mater.*, 2014, **13**, 796-801.
12 H. Wang, T. Kubo, J. Nakazaki and H. Segawa, *Phys. Status Solidi-R*, 2014, **9999**, n/a-n/a.
13 K. W. Johnston, A. G. Pattantyus-Abraham, J. P. Clifford, S. H. Myrskog, D. D. MacNeil, L. Levina and E. H. Sargent, *Appl. Phys. Lett.*, 2008, **92**, 151115.
14 K. S. Leschkies, A. G. Jacobs, D. J. Norris and E. S. Aydil, *Applied Physics Letters*, 2009, **95**, -.
15 A. H. Ip, S. M. Thon, S. Hoogland, O. Voznyy, D. Zhitomirsky, R. Debnath, L. Levina, L. R. Rollny, G. H. Carey, A. Fischer, K. W. Kemp, I. J. Kramer, Z. Ning, A. J. Labelle, K. W. Chou, A. Amassian and E. H. Sargent, *Nat. Nanotech.*, 2012, **7**, 577-582.
16 Z. Ning, Y. Ren, S. Hoogland, O. Voznyy, L. Levina, P. Stadler, X. Lan, D. Zhitomirsky and E. H. Sargent, *Adv. Mater.*, 2012, **24**, 6295-6299.
17 S. M. Thon, A. H. Ip, O. Voznyy, L. Levina, K. W. Kemp, G. H. Carey, S. Masala and E. H. Sargent, *ACS Nano*, 2013, **7**, 7680-7688.
18 J. Zhang, J. Gao, E. M. Miller, J. M. Luther and M. C. Beard, *ACS Nano*, 2013, **8**, 614-622.
19 D. Zhitomirsky, O. Voznyy, S. Hoogland and E. H. Sargent, *ACS Nano*, 2013, **7**, 5282-5290.
20 D. Zhitomirsky, O. Voznyy, L. Levina, S. Hoogland, K. W. Kemp, A. H. Ip, S. M. Thon and E. H. Sargent, *Nat. Commun.*, 2014, **5**, doi:10.1038/ncomms4803.
21 I. J. Kramer, D. Zhitomirsky, J. D. Bass, P. M. Rice, T. Topuria, L. Krupp, S. M. Thon, A. H. Ip, R. Debnath, H.-C. Kim and E. H. Sargent, *Adv. Mater.*, 2012, **24**, 2315-2319.
22 J. Jean, S. Chang, P. R. Brown, J. J. Cheng, P. H. Rekemeyer, M. G. Bawendi, S. Gradečak and V. Bulović, *Adv. Mater.*, 2013, **25**, 2790-2796.
23 H. Wang, T. Kubo, J. Nakazaki, T. Kinoshita and H. Segawa, *J. Phys. Chem. Lett.*, 2013, **4**, 2455-2460.
24 L. Etgar, W. Zhang, S. Gabriel, S. G. Hickey, M. K. Nazeeruddin, A. Eychmüller, B. Liu and M. Grätzel, *Adv. Mater.*, 2012, **24**, 2202-2206.
25 B. Ehrler, K. P. Musselman, M. L. Böhm, F. S. F. Morgenstern, Y. Vaynzof, B. J. Walker, J. L. MacManus-Driscoll and N. C. Greenham, *ACS Nano*, 2013, **7**, 4210-4220.
26 R. L. Z. Hoye, B. Ehrler, M. L. Böhm, D. Muñoz-Rojas, R. M. Altamimi, A. Y. Alyamani, Y. Vaynzof, A. Sadhanala, G. Ercolano, N. C. Greenham, R. H. Friend, J. L. MacManus-Driscoll and K. P. Musselman, *Adv. Energy Mater.*, 2014, doi: 10.1002/aenm.201301544.
27 I. Mora-Seró, S. Giménez, F. Fabregat-Santiago, R. Gómez, Q. Shen, T. Toyoda and J. Bisquert, *Acc. Chem. Res.*, 2009, **42**, 1848-1857.
28 B. A. Gregg, F. Pichot, S. Ferrere and C. L. Fields, *J. Phys. Chem. B*, 2001, **105**, 1422-1429.
29 H. Wang, E. D. Gomez, Z. Guan, C. Jaye, M. F. Toney, D. A. Fischer, A. Kahn and Y.-L. Loo, *J. Phys. Chem. C*, 2013, **117**, 20474-20484.
30 J. Gao, C. L. Perkins, J. M. Luther, M. C. Hanna, H.-Y. Chen, O. E. Semonin, A. J. Nozik, R. J. Ellingson and M. C. Beard, *Nano Letters*, 2011, **11**, 3263-3266.
31 K. W. Kemp, A. J. Labelle, S. M. Thon, A. H. Ip, I. J. Kramer, S. Hoogland and E. H. Sargent, *Adv. Energy Mater.*, 2013, **3**, 917-922.
32 J. Tian, Q. Zhang, E. Uchaker, R. Gao, X. Qu, S. Zhang and G. Cao, *Energy Environ. Sci.*, 2013, **6**, 3542-3547.
33 Z. Tachan, I. Hod, M. Shalom, L. Grinis and A. Zaban, *Phys. Chem. Chem. Phys.*, 2013, **15**, 3841-3845.
34 U. Ozgur, Y. I. Alivov, C. Liu, A. Teke, M. A. Reshchikov, S. Dogan, V. Avrutin, S. J. Cho and H. Morkoc, *J. Appl. Phys.*, 2005, **98**, 041301.
35 R. L. Z. Hoye, K. P. Musselman and J. L. MacManus-Driscoll, *APL Materials*, 2013, **1**, 060701.
36 S. Yodyingyong, X. Zhou, Q. Zhang, D. Triampo, J. Xi, K. Park, B. Limketkai and G. Cao, *J. Phys. Chem. C*, 2010, **114**, 21851-21855.
37 J. Chang and E. R. Waclawik, *J. Nanopart. Res.*, 2012, **14**, 1012.
38 I. Mora-Sero, L. Bertoluzzi, V. Gonzalez-Pedro, S. Gimenez, F. Fabregat-Santiago, K. W. Kemp, E. H. Sargent and J. Bisquert, *Nat. Commun.*, 2013, **4**, 3272.
39 H. Tang, K. Prasad, R. Sanjinès, P. E. Schmid and F. Lévy, *J. Appl. Phys.*, 1994, **75**, 2042-2047.
40 A. Zaban, M. Greenshtein and J. Bisquert, *ChemPhysChem*, 2003, **4**, 859-864.
41 W. B. Berry and P. Longrigg, *Solar Cells*, 1988, **24**, 321-328.
42 I. Mora-Sero, G. Garcia-Belmonte, P. P. Boix, M. A. Vazquez and J. Bisquert, *Energy Environ. Sci.*, 2009, **2**, 678-686.
43 F. Fabregat-Santiago, G. Garcia-Belmonte, I. Mora-Sero and J. Bisquert, *Phys. Chem. Chem. Phys.*, 2011, **13**, 9083-9118.
44 V. Gonzalez-Pedro, E. J. Juarez-Perez, W.-S. Arsyad, E. M. Barea, F. Fabregat-Santiago, I. Mora-Sero and J. Bisquert, *Nano Letters*, 2014, **14**, 888–893.

